Section 1. Ellipsometric Measurement Results of Refractive Indices for the Amorphous and Crystalline States of $Ge_2Sb_2Te_5$

The $Ge_2Sb_2Te_5$(GST) film was initially prepared using the sputtering technique, achieving a thickness of 45 nm, as indicated in the main text. The complex refractive index for both amorphous and crystalline GST films, which includes both the refractive index $\mathrm{n}(\lambda)$ and the absorption coefficient $\kappa(\lambda)$ as functions of wavelength, was measured at room temperature and above the phase transition temperature of approximately 150 ℃using a Mueller Matrix Ellipsometer (ME-L), as shown in Figure S1. To induce crystallization in the GST film, the as-deposited amorphous film was subjected to a thermal treatment at 180 ℃ for 30 seconds.

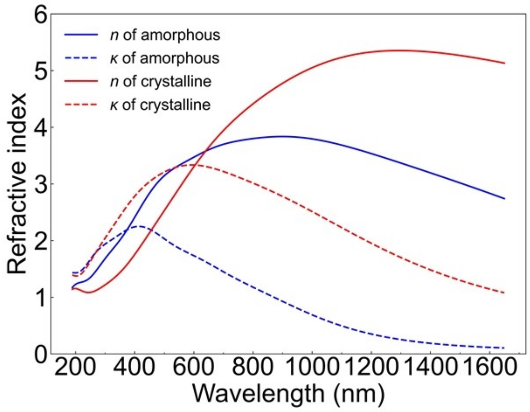

Figure S1. Measured refractive indices over the spectral range from 189 nm to 1650 nm. ration area for evaluating the ER.

Section 2. Ellipsometric Measurement Results of Refractive Indices for the Amorphous and Crystalline States of Ge2Sb2Te5

Zoomed-In Figures of Figure 3 (b-e) in the Main Text

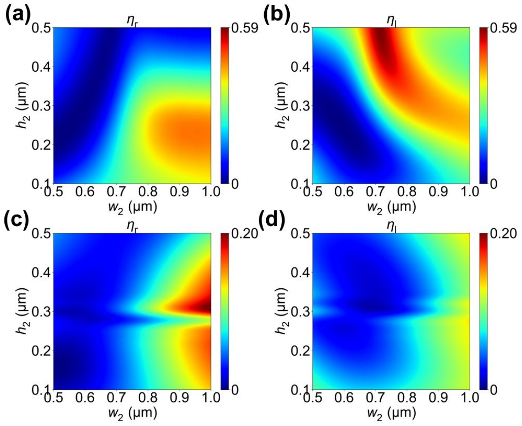

Figure S2 (a) and (b) show the rightward and leftward SPP generation efficiencies for the amorphous GST state, while (c) and (d) show the rightward and leftward SPP generation efficiencies for the crystalline GST state. S2 (a) and (b) are magnifications of Figs. 3 (c) and (d) in the main text, respectively, and S2 (c) and (d) are magnifications of Figs. 3 (e) and (f) in the main text, respectively.

Section 3. Physical Origin of the Refractive Index Dependent Directional Switching

The asymmetric nanogroove structure can be modeled as two Fabry-Pérot (FP) cavities that support several discrete modes. Based on the calculation of TM eigenmodes, both symmetric and asymmetric modes coexist within the grooves, which is the fundamental mechanism driving the unidirectionality. The GST layer at the bottom functions as a tunable reflective mirror and a phase retarder. When modes impinge on the GST film, the bottom reflection dictates the phase and intensity of the cavity modes. Upon the GST phase transition from amorphous to crystalline, its refractive index increases significantly. This change, coupled with the enhanced absorption of crystalline GST, attenuates the mode intensity and modifies the interference conditions, ultimately leading to the observed switching of unidirectionality.

This physical origin is more comprehensively interpreted through a semi-analytical model based on[2]. The results show that as GST transforms from the amorphous to the crystalline state, the reflection amplitude of the groove decreases, leading to a reduction in unidirectionality.

3.1 Waveguide Mode Characterization

First, the modes supported by the grooves are calculated, as these modes dictate the direction of SPP excitation. We consider the nanogrooves as two distinct grooves defined as the main groove and the auxiliary groove, as shown in Figure S3. The main groove is the upper groove, and the auxiliary groove is the lower groove located to the left. For clarity, W_{main}($W_{main} = w_1 + w_2 = 1480nm$,$w_1 = 800\ nm$,$w_2 = 680\ nm$) is the main groove width, and $W_{aux}$is the auxiliary groove width($W_{main} = w_1 = 800nm$).

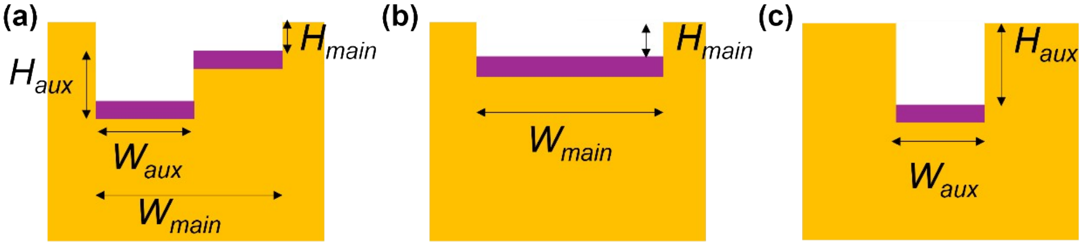

Figure S3. Schematic of the combined two grooves (a), single main groove (b), and single auxiliary groove (c) Yellow denotes Au, and purple denotes GST.

Both grooves can be regarded as vertical metal-dielectric-metal (MDM) waveguides in Figure S4. Schematic of the vertical metal-dielectric-metal structure.. By solving Maxwell's equations, the propagation constants of the main groove and the auxiliary groove can be obtained. Since the Surface Plasmon Polariton (SPP) is excited by TM waves, we only consider the TM mode solutions.

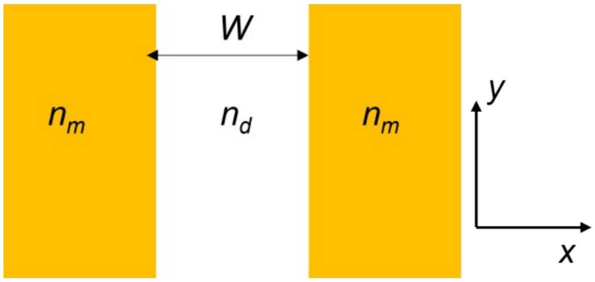

Figure S4. Schematic of the vertical metal-dielectric-metal structure.

The solution equations corresponding to symmetric and anti-symmetric modes are given by equations (1a) and (1b), respectively.

$$\frac{n_d^2\sqrt{n_{eff}^2 - n_m^2}}{n_m^2\sqrt{n_{eff}^2 - n_d^2}} = -tanh(\sqrt{n_{eff}^2 - n_d^2}\,\frac{k_0 w}{2} \tag{1a}$$

$$\frac{n_d^2\sqrt{n_{eff}^2 - n_m^2}}{n_m^2\sqrt{n_{eff}^2 - n_d^2}} = -coth(\sqrt{n_{eff}^2 - n_d^2}\,\frac{k_0 w}{2} \tag{1b}$$

We focus on the operating wavelength of 1510 nm. At this wavelength, the refractive index of gold is n_m = 0.54 + 9.57i, the dielectric is air (n_d=1). The width of the groove determines the modes that can propagate, which subsequently decides the mode interference pattern of the nanogrooves. Only a few waveguide modes can propagate, while others are non-propagating modes; the latter are less important due to their significant propagation losses. The dispersion relations of the main and auxiliary grooves are calculated in Figure S5(a) and (b), respectively. The modes are ordered by their effective refractive index (n_{eff}). For the main groove, there are three propagating modes: the 1st and 3rd are symmetric, while the 2nd is anti-symmetric. The 3rd mode is near the cutoff at $\lambda = 1510$nm. The effective refractive indices are $n_{eff1} =$ 1.0188 + 0.0012i,

$n_{eff2} =$ 0.9015 + 0.0024i and $n_{eff3} =$ 0.1704 + 0.0114i. For the auxiliary groove, there are two propagating modes, the 1st are symmetric, while the 2nd is anti-symmetric. The effective refractive indices are $n_{eff1} =$ 1.0329 + 0.0019i and $n_{eff2} =$ 0.4902 + 0.0077i.

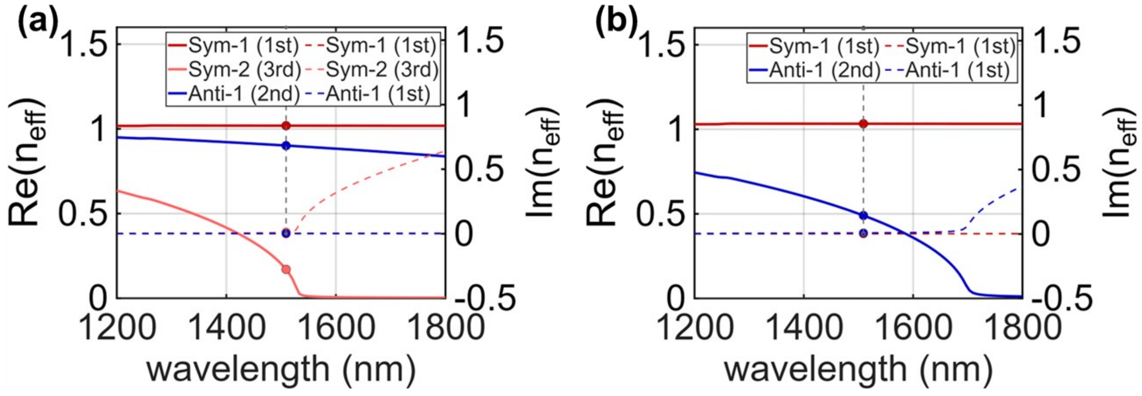

Figure S5. Dispersion relations of the first few modes in the MDM waveguide. The waveguide width is fixed at (a) W_{main}=1480 nm and (b) W_{aux}=800 nm. The 1st, 2nd, and 3rd modes are represented by red, blue, and pink lines, respectively. Solid and dashed lines denote the real part Re(n_{eff}) and imaginary part Im(n_{eff}) of the effective refractive index.

3.2 GST Phase-Change Properties

The covalently bonded amorphous phase of GST can be considered a disordered material with short-range atomic order, low electrical conductivity, and low optical absorption ($\tilde{n}_{amorph} = 2.996 + 0.14i$ at $\lambda = 1.51\mu$m). In contrast, the resonantly bonded crystalline phase behaves like a low-band-gap semiconductor, exhibiting an electrical conductivity three orders of magnitude greater than the amorphous phase and significantly larger optical absorption ($\tilde{n}_{cryst} = 5.257 + 1.279i$ at $\lambda = 1.51\mu$m). In the semi-analytical model, the GST film, situated on the step and at the bottom of the auxiliary groove, is combined with the Au bottom layer to form a reflective mirror that serves as a phase modulator impacting mode interference.

3.3 Three-Stage Semi-Analytical Framework

The excitation of SPPs by the asymmetric grooves can be decoupled into several single steps in Figure S6. In the first stage, normally incident light is focused onto the entrance of the upper main groove; the symmetric 1st mode in the main groove is excited with high efficiency, and a portion of the source is converted into the SPP at the Au-air interface. Here, the excitation coefficient matrices $S_{in,lsp}$ and $S_{in,rsp}$ represent the excitation of leftward and rightward SPPs by the directly incident Gaussian source (waist width = 2μm) , while $S_{in,g1}$(3 × 1 matrix) represents the excitation of waveguide modes in the main groove. In the second step, the excited 1st, 2nd, and 3rd modes in the main groove propagate downward and are reflected at the bottom. This reflection results in upward-propagating 1st, 2nd, and 3rd modes. These three modes then reflect back and forth between the top and bottom of the main groove. The final steady state is described by a self-consistent equation involving I^+ and I^-, which are the upward and downward intensities, respectively. R^{t,g_1} is the top reflection coefficient, and R is the self-consistent stable reflection matrix involving the reflection coefficients of the downward modes, the incident modes converting from the main groove to the auxiliary groove, reflecting at the auxiliary bottom, and then coupling back upward into the main groove after multiple reflections. In the third stage, the upward-propagating 1st, 2nd and 3rd modes in the main groove partly convert into SPPs at the top of the upper main groove. $S^{g_1,lsp}$ and $S^{g_1,rsp}$ are the SPP excitation coefficients by the upward 1st, 2nd and 3rd mode for the left direction and right direction, respectively.

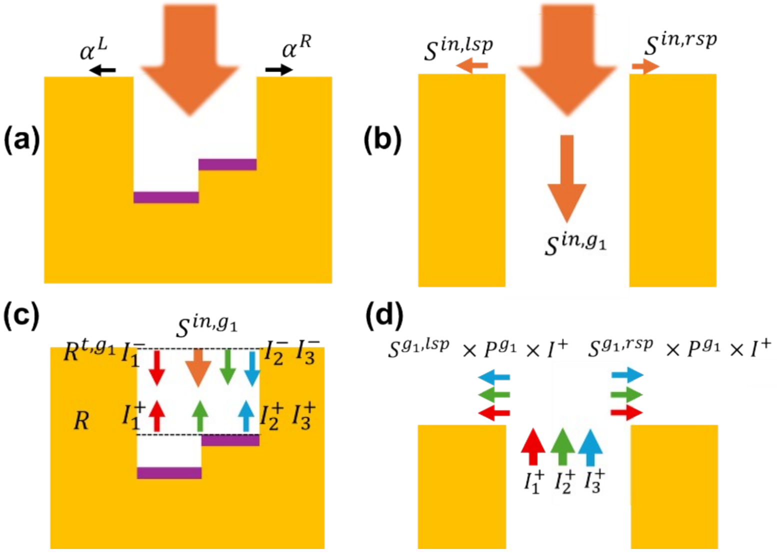

Figure S6. Illustration of the semi-analytical model. (a) SPP excitation by the asymmetric groove. (b) First basic process: normally incident light imping on the entrance of the main groove. (c) Second basic process: reflections and cross-conversions of the 1st, 2nd, and 3rd modes at the top and bottom interfaces of the main groove. (d) Third basic process: upward-propagating 1st, 2nd, and 3rd modes in the main groove partially converting into SPPs at the top of the main groove.

We focus on the leftward and rightward intensities, which determine the unidirectionality. α^L and α^R denote the complex amplitude of the total leftward and rightward SPPs on the front metal surface. These can be decoupled into two main sources: the SPPs excited directly by the incident light, and the SPPs excited by the groove modes converted from the incident source. For the latter, the incident source converts a portion of energy into propagating groove waveguide modes, which propagate a distance h_{main} with the effective refractive index of the corresponding mode number, reflect backward at the groove step with a propagation phase delay, reach the top of the main groove, and finally convert into propagating SPPs along the surface.

This is described by equations (2a) and (2b), where P^{g_1} is the propagation matrix(3 × 3), and the diagonal elements $e^{ik_{iy}^{g_1}h_{main}}$ represent the propagation phase delay of the i-th mode along distance h_{main}.

$$\alpha^L = S^{in,lsp} + S^{g_1,lsp} \times P^{g_1} \times I^+ \tag{2a}$$

$$\alpha^R = S^{in,rsp} + S^{g_1,rsp} \times P^{g_1} \times I^+ \tag{2b}$$

$$P^{g_1} = \begin{pmatrix} e^{ik_{1y}^{g_1}h_{main}} & & \\ & e^{ik_{2y}^{g_1}h_{main}} & \\ & & e^{ik_{3y}^{g_1}h_{main}} \end{pmatrix} \tag{3}$$

The propagation matrix for the auxiliary groove, P^{g_2}, is defined similarly.

$$P^{g_2} = \begin{pmatrix} e^{ik_{1y}^{g_1}h_{aux}} & \\ & e^{ik_{2y}^{g_1}h_{aux}} \end{pmatrix} \tag{4}$$

By solving the coupled-mode equations (5a) and (5b) for the steady-state intensities, we obtain the expression for I^+ in equation (5c) and subsequently for α^L and α^R as shown in equations (6a) and (6b).

$$I^+ = R \times P^{g_1} \times (I^- + S^{in,g_1}) \tag{5a}$$

$$I^- = R^{t,g_1} \times P^{g_1} \times I^+ \tag{5b}$$

$$I^+ = \left(1 - R \times P^{g_1} \times R^{t,g_1} \times P^{g_1}\right)^{-1} \times R \times P^{g_1} \times S^{in,g_1} \tag{5c}$$

$$\alpha^L = S^{in,lsp} + S^{g_1,lsp} \times P^{g_1} \times \left(1 - R \times P^{g_1} \times R^{t,g_1} \times P^{g_1}\right)^{-1} \times R \times P^{g_1} \times S^{in,g_1} \tag{6a}$$

$$\alpha^R = S^{in,rsp} + S^{g_1,rsp} \times P^{g_1} \times \left(1 - R \times P^{g_1} \times R^{t,g_1} \times P^{g_1}\right)^{-1} \times R \times P^{g_1} \times S^{in,g_1} \tag{6b}$$

3.4 Formulation of the Reflection Matrix R

The reflection matrix R depicts the mode reflection and cross-conversion at the bottom of the main groove. The total reflected field amplitudes consist of two coherent components: direct reflection from the step junction and the reflection from the auxiliary groove, where modes from the main groove propagate through the auxiliary cavity and reflect.

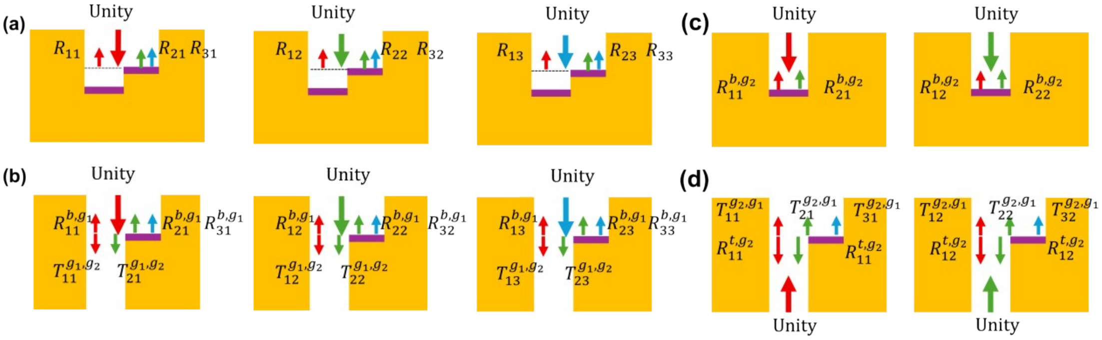

Figure S7. Illustration of the basic scattering processes for calculating R. The 1st, 2nd and 3rd modes are indicated by red, green and blue arrows, respectively. (a) Mode reflections at the bottom of the main groove with a finite-depth auxiliary groove. (b) First process: Mode reflections and transmissions at the interface of the main groove assuming an infinitely deep auxiliary groove. (c) Second process: Propagation and reflection of the 1st and 2nd modes within the auxiliary groove (groove 2). (d) Third process: Reflection and transmission of the 1st and 2nd mode at the top interface of groove 2, assuming an infinitely long main groove above.

This can be decoupled into multiple basic scattering processes in Figure S7 First, a downward mode propagates to the bottom of the main groove and is partly reflected upward and partly transmitted into the auxiliary groove (groove 2). This is described by a reflection matrix R^{b,g_1}(3 × 3) and a transmission matrix T^{g_1,g_2}(2 × 3). Second, the transmitted modes propagate in the auxiliary groove and reflect at its bottom, represented by propagator P^{g_2} and reflection coefficient R^{b,g_2}. Third, the upward modes in groove 2 are partly reflected at the top of groove 2 and partly transmitted back into the upper main groove, with coefficients R^{t,g_2} and T^{g_2,g_1}. The round-trip propagation operator in the auxiliary groove is defined as L:

$$L = R^{t,g_2} P^{g_2} R^{b,g_2} P^{g_2} \tag{7}$$

The steady-state field involves the summation of infinite round trips,

$$\sum_{n=0}^{\infty} L^n = (1 - L)^{-1} \tag{8}$$

forming a geometric series $(1-L)^{-1}$. The contribution from the auxiliary groove R_{g_2} is

$$R_{g_2} = T^{g_2,g_1} \times (1 - L)^{-1} \times P^{g_2} \times R^{b,g_2} \times P^{g_2} \times T^{g_1,g_2} \tag{9}$$

$$R_{g_2} = T^{g_2,g_1} \times \left(1 - R^{t,g_2} P^{g_2} R^{b,g_2} P^{g_2}\right)^{-1} \times P^{g_2} \times R^{b,g_2} \times P^{g_2} \times T^{g_1,g_2} \tag{10}$$

Therefore, the total reflection matrix R is given by equation (12), which is the sum of R^{b,g_1} and the contribution from the auxiliary groove R_{g_2}.

$$R = R^{b,g_1} + R_{g_2} \tag{11}$$

$$R = R^{b,g_1} + T^{g_2,g_1} \times \left(1 - R^{t,g_2}P^{g_2}R^{b,g_2}P^{g_2}\right)^{-1} \times P^{g_2} \times R^{b,g_2} \times P^{g_2} \times T^{g_1,g_2} \tag{12}$$

The reflection matrix R incorporates both self-reflection (where a mode reflects into itself) denoted by R_{ii}(i=1,2,3) and mode conversion (where one mode is reflected into another) denoted by R_{ij}(i $\neq$ j,i,j=1,2,3).

3.5 Model Validation and Fabry-Peot Resonance

We then used the semi-analytical model to calculate the coefficients discussed above and obtained the leftward intensity I_L ($|\alpha^L|^2$) and rightward intensity I_R ($|\alpha^R|^2$) for both amorphous and crystalline states. Figure S8 illustrates the intensities of rightward and leftward SPPs as functions of h_{main} and h_{aux}. The widths of the main groove and auxiliary groove are fixed to $w_{main} = 1480nm$ and $w_{aux} = 800nm$, the incident wavelength is set to λ=1510 nm. Figure S8 (a-b) and Figure S8 (c-d) show the results for the amorphous state calculated by the semi-analytic model and direct FDTD simulation, respectively. Similarly, the semi-analytic and FDTD results for the crystalline state are presented in Figure S8 (e-f) and Figure S8 (g-h). The black dots represent the design points.

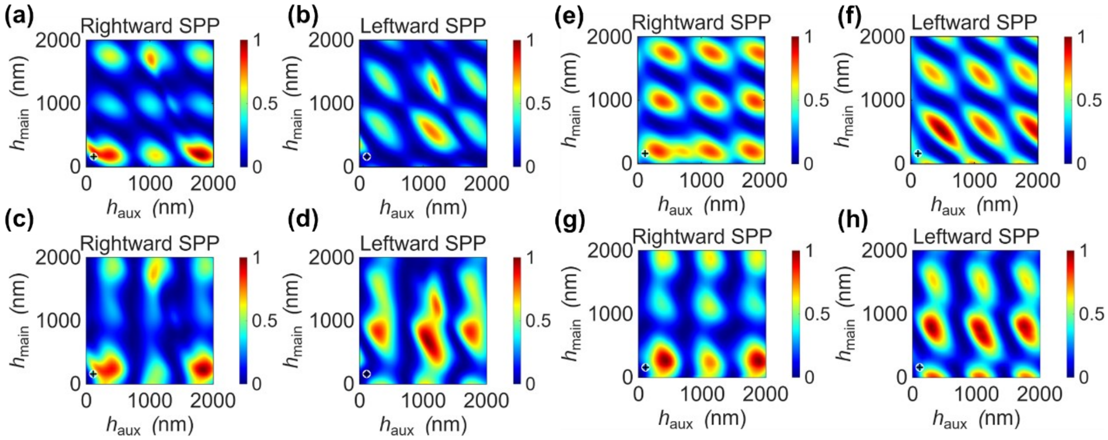

Figure S8. Rightward and Leftward SPP intensities as functions of h_{main} and h_{aux} for amorphous state and crystalline state. (a) and (b) show calculation results by the semi-analytical model, while (c) and (d) show direct simulation results for the amorphous state. (e) and (f) show calculation results by the semi-analytical model, while (g) and (h) show direct simulation results for the crystalline state. The black cross denotes the position of the design parameters.

The semi-analytical model shows a similar periodicity to the direct FDTD results. The periods of the leftward and rightward intensities are about 775 nm and 779 nm, respectively. These values lie between the FP periods of the 1st and 2nd modes ($P_1 = \dfrac{\lambda}{2n_{eff1}} = 741$ nm, $P_2 = \dfrac{\lambda}{2n_{eff2}} = 838$ nm), indicating that the 1st and 2nd modes dominate the FP resonance. Both the rightward and leftward intensities include the 1st and 2nd modes.

3.6 Absorption-Driven Switching

The ratio between the 1st-mode upward intensity I_1^+ and the 2nd-mode intensity I_2^+ determines the directionality, which is controlled by the reflection coefficients($R_{11}R_{12}$,etc.). It can be seen from Figure S8 and Figure S8 (g–h) that the peak positions almost remain unchanged from the amorphous state to the crystalline state. This can be explained by the reflection matrix R. As shown in Figure S9(e), the oscillation periods and the positions of peaks and valleys remain largely aligned between the two states, indicating that the phase condition is primarily determined by the h_{aux}rather than the GST phase transition.

While in Figure S9 amplitudes of the R coefficients significantly decrease as GST changes from amorphous to crystalline. Notably, $|R_{21}|$ exhibits near-unity efficiency (~1.0) in the amorphous state, however, this conversion efficiency drops to ~0.6 in the crystalline state, limiting the mode conversion. Thus, amplitude balance between interacting modes required for high ER ratios are disrupted and the unidirectionality is diminished. In Figure S9(c) to (d), the ER distribution remains almost the same when transitioning from amorphous to crystalline, but the absolute values decrease. In conclusion, the main reason that leads to the unidirectionality switch is the GST optical absorption.

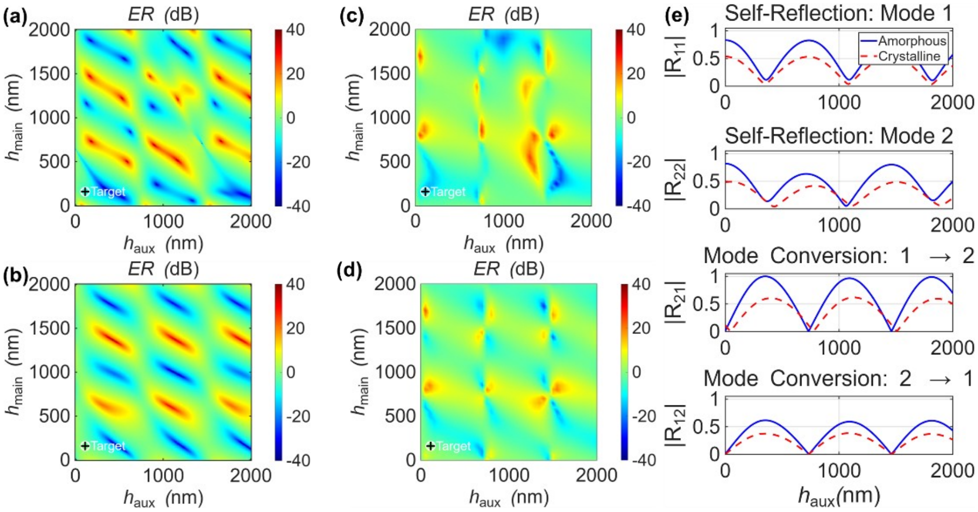

Figure S9. Extinction ratio (ER) as a function of h_{aux} and h_{main} for amorphous and crystalline states. (a–b) Semi-analytical results and (c–d) direct FDTD simulation results. The black cross denotes the position of the design parameters. (e) Amplitude of reflection R coefficients for amorphous and crystalline states.

Section 4. The Impact of Au Layer Thickness on the ER

In our design featuring two nanogrooves, the left nanogroove has a depth h_1= 270 nm. Given that the total Au layer thickness is 300 nm, the remaining gold thickness beneath the left nanogroove is approximately 30 nm. The structure with the two nanogrooves with the left nanogroove of h_1 = 270 nm, since the Au layer thickness is 300 nm, the gold layer beneath the left nanogroove is approximately 30 nm. The thickness is roughly 2.7 times the skin depth (d= $\lambda/4\pi$k) at our operating wavelength 1510nm. At this thickness, the metal film does not provide perfect screening for the electromagnetic field. As visualized in our simulations (Figure S10), a small portion of the optical energy leaks through this thin region into the substrate, especially when compared to the structure with a thicker Au layer shown in Figure S10 (b). Due to this partial energy leakage into the substrate, the Extinction Ratio (ER) exhibits a degradation of approximately 1.5 dB, as shown in Figure S11. However, we consider this degradation to be negligible in comparison to the device's high overall directivity.

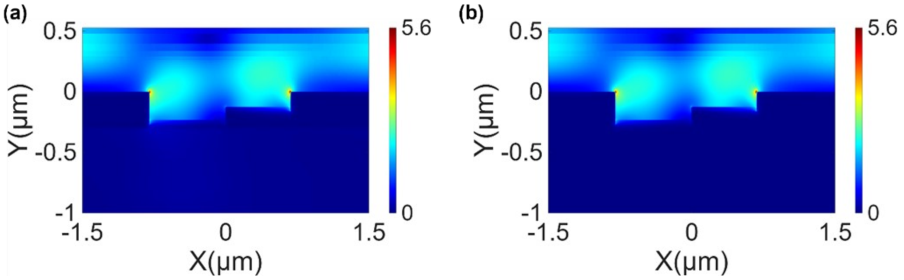

Figure S10. Electric Field Amplitude for (a) 300 nm-thick Au Film and (b) 3 μm-thick Au Film.

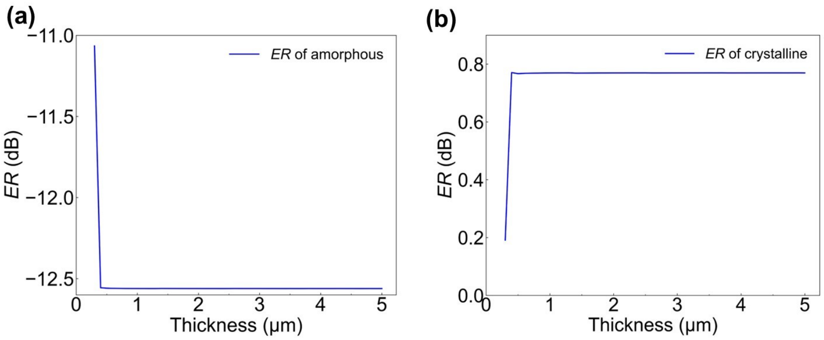

Figure S11. ER as a function of Au layer thickness from 20 nm to 5 μm at (a) amorphous state and (b) crystalline state.

Section 5. Measurement of Pulse Power and System Optical Loss when Illuminated on the Sample

To accurately determine the pulse power illuminated on the sample, the polarizer and half-wave plate were removed from the optical path. A microscope slide power sensor (S17C, Thorlabs) was then used to measure the power transmitted through the variable neutral density (ND) filter (NDC-25C-2M-A, Thorlabs) and the focus objective lens. The variable ND filter provides adjustable attenuation via rotation, enabling precise control over the incident power. The average measured output power of the laser (NPL52C, Thorlabs) was found to be approximately 9 mW. Considering the pulse width of 129 ns and the corresponding frequency of 50 kHz, we use the formula $\mathrm{P}_{\mathrm{peak}} = \frac{\mathrm{P}_{\mathrm{avg}} \times \mathrm{T}}{\tau_{\mathrm{pulse}}}$, where the $\mathrm{P}_{\mathrm{peak}}$ is the peak power, $\mathrm{P}_{\mathrm{avg}}$ is the average power, T is the period, and $\tau_{\mathrm{pulse}}$is the pulse width. The calculated output peak power of the laser is approximately 1400 mW.

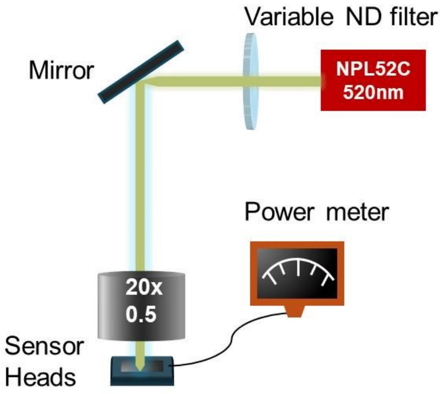

Figure S12. Setup for measuring pulse power delivery to the sample plane.

The average power transmitted through the objective lens was measured to be approximately 3.71 mW in the absence of the neutral density (ND) filter. Applying the formula $P_{peak} = \frac{P_{avg} \times T}{\tau_{pulse}}$ yielded a calculated peak power of 570 mW. The optical system path loss was estimated to be approximately 0.6. This allows for precise modulation of the peak pulse power using the variable ND filter, enabling a wide dynamic range of 0 - 570 mW. During the switching experiments, the pump energy can be fine-tuned using the variable ND filter, whose transmission coefficient ((T_{ND}) was calculated based on its rotation angle according to the manufacturer's standard formula: $\mathrm{T}_{ND} = 10^{-OD(\theta)}$ Here, the optical density is defined as OD(θ) = m·ϑ, where m =0.00741 and θ is the angle in degrees). Therefore, the exact single-pulse energy delivered to the sample for each data point was calculated using the equation $E_{pulse} = P_{peak\_source} \cdot \eta_{sys} \cdot \mathrm{T}_{ND} \cdot \tau$. This calibrated approach ensures the accuracy of the experimental energy values by accounting for all actual system losses. This calibrated pulse power setup enables the precise control of pulse energy required for the experiments.

Section 6. Thermal Analysis of Heat Dissipation, Temperature Distribution, and Switching Dynamics

6.1 Time-resolved Thermal Simulations of the Switching Processes.

we simulated the amorphous-to-crystalline (SET) process and the crystalline-to-reamorphized (RESET) process, as shown in Figure S13(a) and Figure S13 (b), respectively. For the crystallization process, a pulse of 37 mW and 129 ns was applied. Figure S13(a) demonstrates that the GST temperature rises above the crystallization threshold (~423 K) and subsequently cools down within a few hundred nanoseconds. For the reamorphization process, a pulse of 175 mW and 29 ns was utilized. As shown in Figure S13(b), the temperature rapidly increases to 882 K, which is above the amorphization temperature of GST (~873 K). Reamorphization typically requires fast quench rates on the order of 10^9 K/s. In our simulation, the calculated quench rate is approximately 6.3×10^{10} K/s, which exceeds the requirement for fast quenching. These simulation results provide robust evidence that the device can operate within the nanosecond regime.

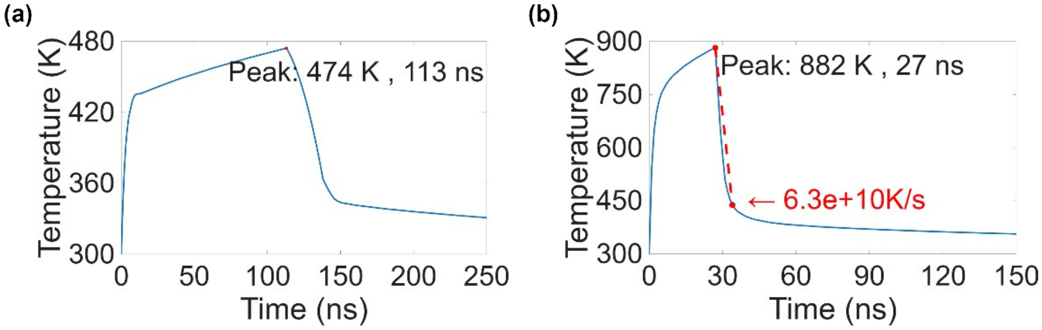

Figure S13. Time-resolved thermal simulations of the switching processes. (a) Temporal evolution of the peak temperature in the GST layer under a 37 mW, 129 ns laser pulse (Amorphous-to-Crystalline process). (b) Temporal evolution of the peak temperature in the GST layer under a 175 mW, 29 ns laser pulse (Crystalline-to-Reamorphized process).

6.2. Temperature Calculation for Different Cumulative Energy Input of the Pulsed Laser

Thermal simulations modeling the amorphous-to-crystalline phase transition were performed to calculate the local temperature as a function of the cumulative energy used in the experiments. The results are illustrated in Figure S14. Since the pump source to stimulate the phase transition of GST is a Gaussian source, the temperature distribution is not uniform, and there exists a temperature difference across the same GST film in the nanogrooves. In Figure S14(a), the maximum temperature of the GST is shown. It reveals that when the cumulative energy reaches about 3.5 nJ, the maximum temperature is above the phase transition temperature (~423 K). This indicates that the GST starts to crystallize, which coincides with the cumulative energy of 2.68 nJ at which the unidirectionality starts to change in the manuscript. However, as shown in Figure S14(b), which presents the minimum temperature as a function of cumulative energy, the minimum temperature is still below the transition temperature when the cumulative energy reaches about 3.5 nJ. This suggests that there still exists amorphous GST within the film. To explore the crystallization ratio change with cumulative energy, we define the Ratio $= \frac{\iiint_{T>423k} dV}{\iiint_{total} dV}$, representing the volume where the temperature is above the transition divided by the total volume, as shown in Figure S14(c). It illustrates that the GST completes full crystallization when the accumulated energy reaches about 13.5 nJ. This coincides with Figure 6 of the manuscript, which shows that the intensity starts to saturate when the energy reaches 15 nJ.

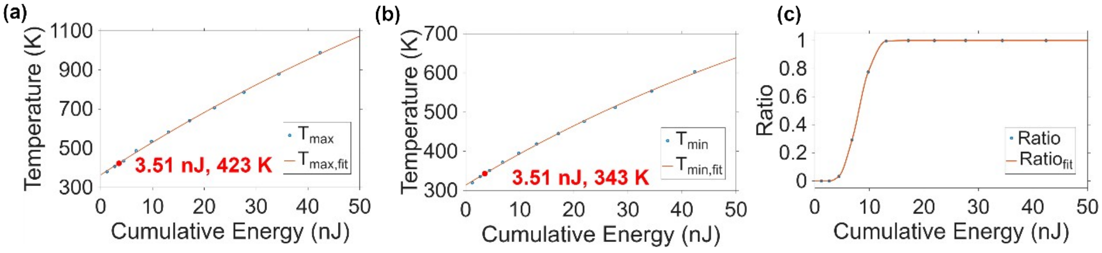

Figure S14. Simulated temperature of the GST film as a function of cumulative energy for (a) maximum temperature, and (b) minimum temperature. (c) Crystallization ratio of the GST film as a function of cumulative energy.

6.3. Photothermal analysis of GST on Au under high-power pulse excitation (122 mW, 29 ns)

The time-resolved thermal simulation is shown in Figure S15. These simulations track the temperature profile of the device cross-section at various time intervals (1 ns, 3 ns, 27 ns, and 150 ns) during a 122 mW, 29 ns pulse. As shown in Figure S15, as time progresses, the thermal energy remains largely confined within the GST layer. The temperature increases as the pulse duration proceeds from 0 to 29 ns and subsequently decreases once the pulse is turned off. At t=27ns, the maximum temperature of the surrounding Au film reaches approximately 417 K. The peak temperature of the Au film (~417 K) is far below the melting point of gold (~1337 K), effectively preventing the Au from melting or diffusing into the GST layer. Additionally, Figure S15 (c) illustrates that the heat dissipation into the Au surface is limited to a lateral distance of about 5 µm. Owing to the nanosecond timescale of the overall heating and cooling process, the thermal energy is localized and does not have sufficient time to penetrate significantly downward or spread to adjacent components.

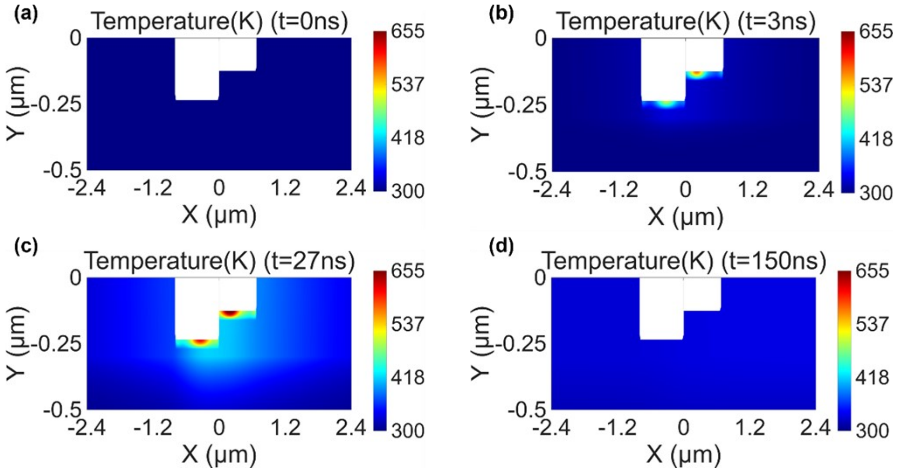

Figure S15. Time-resolved thermal simulation of the device cross-section under a high-power (122 mW, 29 ns) heating pulse. The temperature profiles are shown at (a) t=1 ns, (b) t=3 ns, (c) t=27 ns, and (d) t=150 ns.

Section 7. Simulations for the Sample Measured in Figure 7 of the Main Text.

The designed geometric parameters are as follows: w_1=750nm, w_2=700nm, h_1=250nm, h_2=140nm, and h_3=45nm. At a wavelength of 1510 nm, the ER for the amorphous state is approximately -9.8dB, while for the crystalline state, the ER is about 11.3 dB.

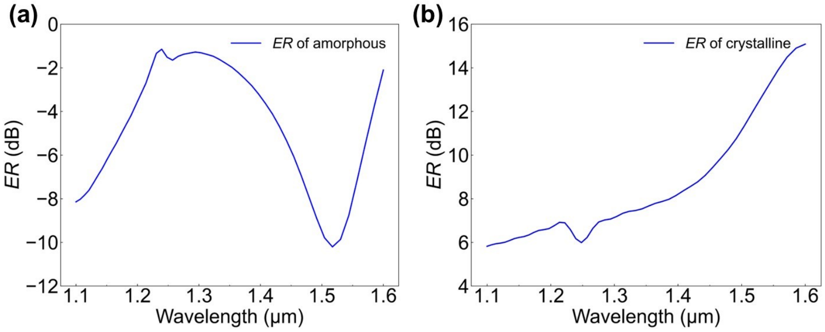

Figure S16. Simulated extinction ratio (ER) versus wavelength for the amorphous and crystalline states.

Section 8. Error Analysis of the Two Designated Geometric Parameters

For the sample($w_1 = 750$nm, $w_2 = 700$ nm, $h_1 = 250$nm, and $h_2 = 140$nm), a systematic tolerance analysis focusing on the realistic geometric deviations introduced during fabrication is performed. Our results indicate that the performance is primarily governed by the GST film thickness and the FIB-induced nanohole span. Based on SEM measurements in Figure S17 we identified several geometric deviations between the design and the fabricated device. The analysis is based on the model in Figure S18

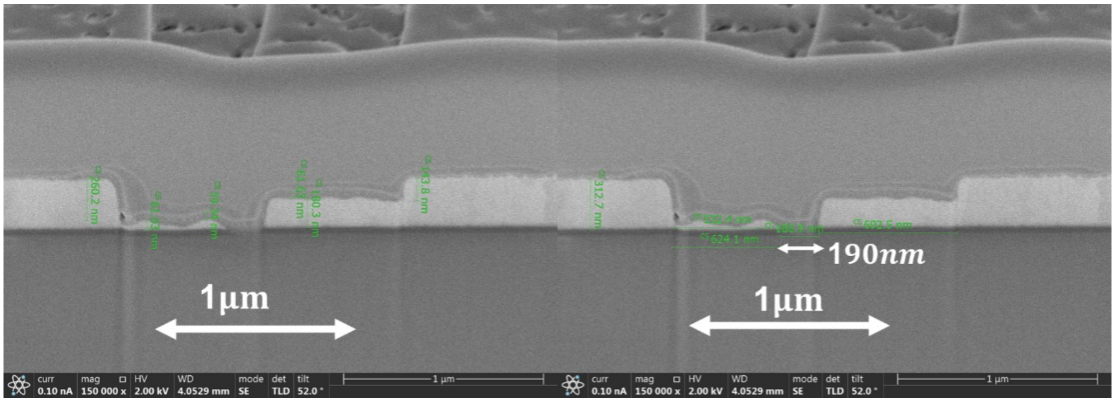

Figure S17. Cross-sectional SEM image of the designed sample (nm, nm, nm, and nm). The measured parameters are: nm, nm, nm, and nm

1) GST thickness: GST thickness increased from the designed 45 nm to the measured 60 nm.

2) Groove Width (w_1,w_2): measured at 750/700nm compared to the designed 718/693nm.

3)Nanohole span: FIB processing introduced a lateral gap (nanohole) of approximately 200nm.

4) Etch depths ((h_1,h_2): Slight variations existed (measured at 260/143nm compared to the designed 250/140nm).

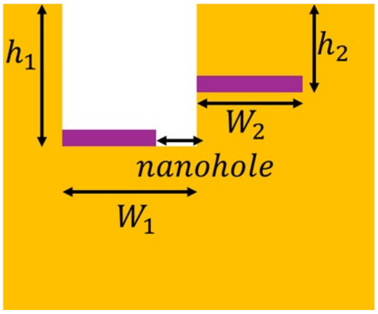

Figure S18. Structural model for error tolerance analysis, with an introduced nanohole.

The amorphous and crystalline states are analysed respectively:

8.1 Crystalline State

For the crystalline state, the experimental ER (~5 dB) is lower than the ideal simulated ER (~11.3 dB). As shown in Figure S19, the increase in GST thickness from the designed 45 nm to the measured 60 nm shifts the device's operating point to the falling edge of the resonance both for the designed and measured parameters in Figure S19 (a) and Figure S19 (b), respectively. In addition, Figure S19(a) and (b), an increase in the nanohole span from 0 nm to 200 nm results in an ER degradation of approximately 1.8 dB for both simulated and experimental parameters at a GST thickness of 60 nm. This reduction is relatively small compared to the variations induced by changes in the GST thickness. Thus, the primary cause of the degraded ER in the crystalline state is the increased GST thickness, which shifts the device's operating point away from resonance.

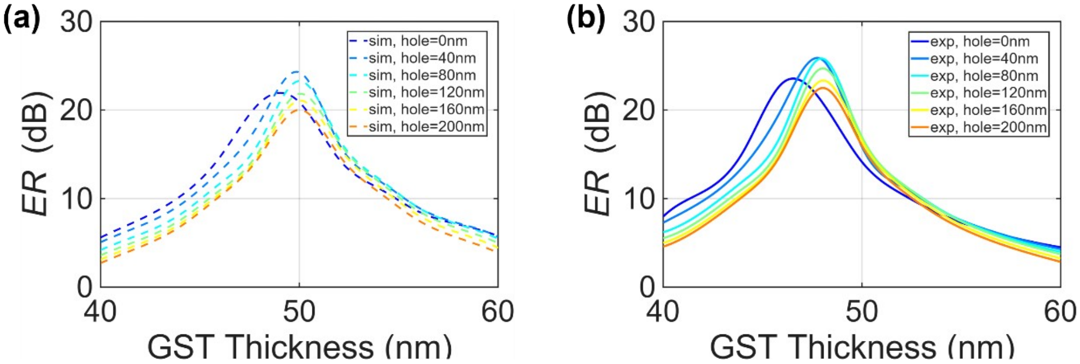

Figure S19. Comparison of the ER as a function of GST thickness between simulated (dashed lines) and experimental (solid lines) results for various nanohole spans for the crystalline state. The experimental data corresponds to fixed widths of $w_1 = 718\mathrm{nm}$, $w_2 = 693\mathrm{nm}$, depths of $h_1 = 260\mathrm{nm}$, $h_2 = 143\mathrm{nm}$, while the simulation uses $w_1 = 750\mathrm{nm}$, $w_2 = 700\mathrm{nm},\ h_1 = 250\mathrm{nm}$ and $h_2 = 140\mathrm{nm}$.

8.2 Amorphous State

For the amorphous state, the experimental ER (~-10.8 dB) is close to the ideal simulated ER (~ -9.8 dB). As shown in Figure S20, if we only consider the increase in GST thickness from 45 nm to 60 nm with an ideal nanogroove structure without nanoholes (nanohole=0nm), the $|ER|$ drops from 9.8 dB to approximately 4.7 dB. Like crystalline state, the increase in GST thickness introduces a phase shift that disrupts the optimal interference condition. The phase mismatch leads to a decline in $|ER|$. However, the FIB-induced nanohole acts as a compensatory role. As shown in Figure S20, as the nanohole span increases from 0 nm to 200 nm, the $|ER|$ increases steadily. The nanohole modifies the local boundary conditions at the groove's base, thereby changing the effective propagation length and the complex reflection coefficients for various modes. This fundamentally alters the modal overlap and consequently shifts the amplitude and phase balance between the symmetric and anti-symmetric modes (a critical factor in controlling the resulting SPP directionality). (as mentioned in Section 3), thereby shifting the mode balance. This suggests that the nanohole introduces a phase shift that effectively counteracts and compensates for the phase error induced by the 60 nm thickened GST film.

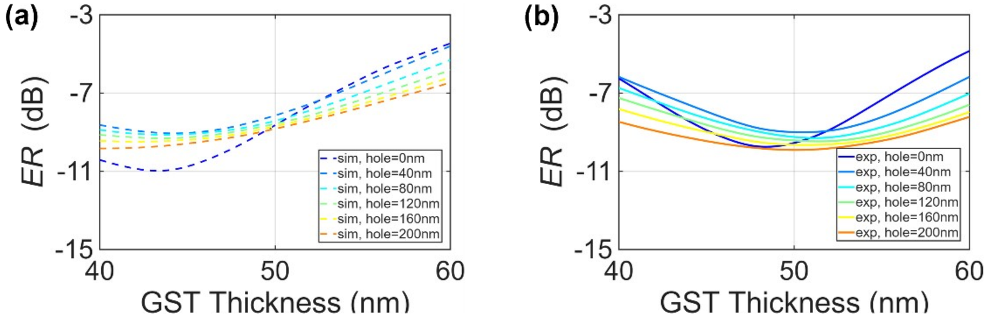

Figure S20. Comparison of the *ER* as a function of GST thickness between simulated (dashed lines) and experimental (solid lines) results for various nanohole spans for the amorphous state. The experimental data corresponds to fixed widths of $w_1 = 718\mathrm{nm}$, $w_2 = 693\mathrm{nm}$, depths of $h_1 = 260\mathrm{nm}$ and $h_2 = 143\mathrm{nm}$, while the simulation uses $w_1 = 750\mathrm{nm}$, $w_2 = 700\mathrm{nm},\ h_1 = 250\mathrm{nm}$ and $h_2 = 140\mathrm{nm}$.

Section 9. Reversible Switching of Phase State of GST Film

We experimentally demonstrate the reversible switching capability of our proposed GST-based plasmonic nano-grooves structure by implementing "write" (crystallization) and "erase" (amorphization) processes on a 45-nm-thick GST film deposited on an Au layer. The polarizer and half-wave plate were removed from the optical path when pumping because the polarizer and half-wave plate attenuated pulse energy too much when generating a pulse onto the sample. A microscope slide power sensor (S17C, Thorlabs) is used to measure the power transmitted through the variable neutral density (ND) filter (NDC-25C-2M-A, Thorlabs) and focus objective lens. To achieve crystallization, we employ a nanosecond pulse laser (NPL52C, Thorlabs) with a pulse width of 129 ns, a frequency of 50 kHz, and a peak power of 31 mW. which falls within the previously reported range of 20 ns to continuous waves, and a power range of 5 mW to 30 mW[3]. Firstly, we selectively crystallize a $100 \times 100\ \mu\mathrm{m}^2$ area of the amorphous film using a pump laser controlled by a PI Objective scanning system (Physik Instrumente) with the pulse power condition mentioned above. The sample was imaged using the reflection optical path on an Olympus optical microscope. This crystallized region exhibits a higher reflection, appearing lighter than the surrounding amorphous film due to the increased reflectivity of the crystalline phase[4]. Subsequently, we amorphized small areas ($1.6\ \mu m \times 3.7\ \mu m$) using a single pump laser pulse with a power of 122 mW and a shorter pulse width of 29 ns, as indicated by the rectangle (c1.1) of the upper subfigure in Figure S21(c). The amorphized region changes to dark, signifying a successful switching of the GST phase from crystalline to amorphous.

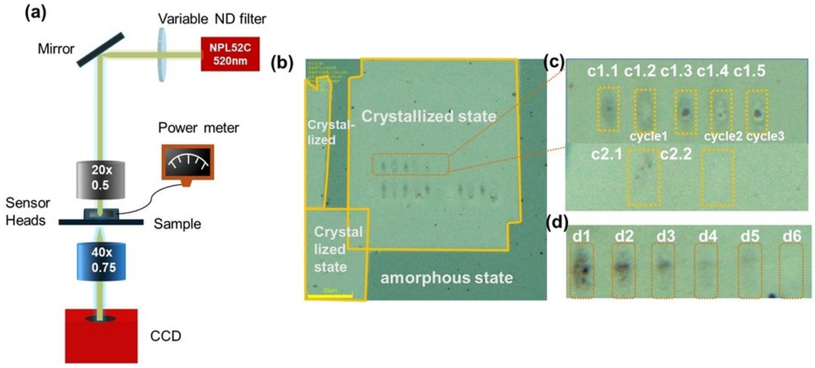

Figure S21.Experimental Investigation of Reversible Phase Switching in $Ge_2Sb_2Te_5$ (GST) Thin Films. (a) Experimental Setup: Schematic diagram illustrating the comprehensive experimental configuration for investigating phase transition dynamics in GST, including laser writing and characterization systems. (b) Cyclic Phase Switching Demonstration: sequential pump pulse impingement on the GST film to systematically validate its reversible switching capability, showcasing the material's reproducible phase transformation potential. In (c), the upper panel (c1) presents a magnified view of the critical transformation region from the rectangular area in (b). The lower panel (c2.1) displays a re-amorphized spot generated by a single 44.1 mW pulse (29 ns duration) applied at 0.5 μm intervals across eight points. The adjacent panel (c2.2) demonstrates a complete cycle of re-amorphization and recrystallization, achieved with a 44.1 mW pulse (29 ns) followed by an 18.8 mW pulse (129 ns), confirming a reversible phase change without ablation. (d) Re-amorphization with Varying Pulse Energies: the re-amorphization of the GST film was achieved using different pulse energies.

Subsequently, rectangle (c1.2) demonstrated a complete cycle: re-amorphization with a single 122 mW, 29 ns pulse, followed by a single crystallization with an 18.8 mW, 129 ns pulse. The area successfully transitioned from crystallized to re-amorphized and back to crystallized. Then, in the rectangle (c1.3), a sequence of pulses was applied: 122 mW, 29 ns → 18.8 mW, 129 ns → 122 mW, 29ns. This resulted in re-amorphization, with a notable black spot due to ablation caused by multiple pulsed laser pumping. Two full cycles were performed on the area in rectangle (c1.4) using the following pulse sequence: (1) 122mW, 29 ns → 18.8 mW, 129 ns → 122 mW, 29 ns. (2) 148.8 mW, 129 ns. The ablation spot shrank after the crystallization pulse, and the area became light-colored, indicating successful crystallization. Then, in rectangle (c1.5), three full cycles were performed. Although there were light spots present, the central area was darkened by ablation after the third cycle. This was attributed to the accumulation of pulse energies and the Gaussian-like source shape, leading to non-uniform energy distribution. The size of the ablation area increased after the final cycle. In Figure S21 (c2.1), a re-amorphization experiment was conducted using a single laser pulse with a power of 44.1 mW and a pulse width of 29 ns. The laser was systematically moved, creating 8 adjacent points with 0.5 μm spatial intervals. Notably, there was no ablation observed. Subsequently, in Figure S21(c2.2), a complete cycle was achieved through a precise two-pulse sequence: a 44.1 mW pulse with a duration of 29 ns, followed by an 18.8 mW pulse with a duration of 129 ns. Under the amorphization pulse power of 44.1 mW, the entire cycle was successfully executed without inducing ablation. Figure S21(d) illustrates the re-amorphization of GST film achieved using different pulse energies. Specifically, the pulse powers employed in the rectangles (d1) through (d5) are 73.6 mW, 62.0 mW, 52.3 mW, 44.1 mW, and 62.0 mW, respectively. Notably, rectangle (d6) demonstrates the re-amorphization achieved with a pulse power of 62.0 mW, followed by an overlaid crystallization pump of 18.8 mW, resulting in a remarkably clean erasure (crystallization) of the sample. It is essential to acknowledge that the energy incident on the sample may exhibit slight instabilities due to focus errors inherent to the experiment setup.

Section 10. Modulation Efficiency Conversion Formula

The term modulation efficiency (η) is used to quantify the modulation depth, which represents the fraction of optical power that can be successfully modulated relative to the maximum power. This is defined by the standard formula:

$$\eta = \left(1 - \frac{I_{min}}{I_{max}}\right) \times 100\% \tag{13}$$

Where $I_{\max}$ corresponds to the optical power in the "On" state(the amorphous state, represented as $\frac{I_{l,amor}}{I_{r,amor}}$), $\mathrm{I}_{\min}$ corresponds to the optical power in the "Off" state(the crystalline state, represented as $\frac{I_{l,cry}}{I_{r,cry}}$). Since the ER is defined as $ER = 10\log_{10}(\mathrm{I}_{\mathrm{l}}/\mathrm{I}_{\mathrm{r}})$, The extinction ratio contrast (ΔER) is related to the ratio of $\mathrm{I}_{\max}$ and $\mathrm{I}_{\min}$ as:

$$\Delta ER = |ER_{amor} - ER_{cry}| = |10\log_{10}\frac{I_{max}}{I_{min}}| \tag{14}$$

From the ΔER value of 15 dB, we can calculate the ratio $\frac{I_{\min}}{I_{\max}}$ and subsequently compute the modulation efficiency. We find that:

$$\frac{I_{\min}}{I_{\max}} = 10^{-\frac{\Delta ER}{10}} = 10^{-1.5} \approx 0.0316 \tag{15}$$

Substituting this ratio into the modulation efficiency formula:

$\eta = (1-0.0316) \times 100\% \approx 96.8\%$Thus, the modulation efficiency is 96.8%, as reported.

References

1. J.-Y. Cho, D. Kim, Y.-J. Park, T.-Y. Yang, Y.-Y. Lee and Y.-C. Joo, Acta Materialia, 2015, 94, 143–151.

2. Yao, W., Liu, S., Liao, H., Li, Z., Sun, C., Chen, J., & Gong, Q. (2015). Efficient Directional Excitation of Surface Plasmons by a Single-Element Nanoantenna. Nano Letters, 15(5), 3115～3121.

3. N. M. Tolkach, P. I. Lazarenko, N. V. Vishniakov and A. D. Maslov, in 2020 IEEE Conference of Russian Young Researchers in Electrical and Electronic Engineering (EIConRus), IEEE, St. Petersburg and Moscow, Russia, 2020, pp. 2208–2211.

4. P. Singh, A. Singh, N. Kanda, et al., "High transmittance contrast in amorphous to hexagonal phase of Ge2Sb2Te5: reversible nir-window," Appl. Phys. Lett. 111 (2017).